FLOW SIMULATION OVER A COMPLETE SATELLITE LAUNCHER WITH A CLUSTER CONFIGURATION

João L.F. Azevedo , Edson Basso , Leonor Camila Q. Yagua , Alexandre P. Antunes
Instituto de Aeronáutica e Espaço
Centro Técnico Aeroespacial
CTA/IAE/ASE-N
12228-904 – São José dos Campos – SP – Brazil
azevedo@iae.cta.br, basso@iae.cta.br, camila@aer.ita.cta.br, alex@iae.cta.br

Keywords: *CFD, Satellite launcher, Euler equations, Chimera technique*

Abstract

The paper is concerned with the development and validation of a 3-D flow simulation capability which would allow the calculation of flowfields over realistic launch vehicle configurations. The formulation here implemented uses the Chimera technique together with block structured grids to discretize the computational domain. The current approach is based on the solution of the 3-D Euler equations in curvilinear coordinates. A finite difference method is applied to these equations and a centered spatial discretization is used. Artificial dissipation terms, based on a scalar, non-isotropic model, are added. The time march process is accomplished with a 5-stage, 2nd-order accurate, Runge-Kutta scheme. The methodology is validated through the simulation of flows inside a 3-D convergent-divergent nozzle within which a cylinder has been inserted. The simulation capability is applied to study the flowfield over the first Brazilian Satellite Launch Vehicle, VLS, during its first-stage flight. VLS results are compared to available experimental data.

1 Introduction

A substantial amount of work in the institutions here represented has been devoted to the development of reliable computational tools for flow simulation in the context of the aerodynamic and aerothermodynamic design of the VLS system, the first Brazilian satellite launcher. Examples of this development work can be found in Refs. [1]–[4]. The VLS has a fairly complex configuration, consisting of four strap-on boosters around a central core and with a hammerhead-type payload shroud. A schematic representation of the vehicle is presented in Fig. 1. For such a configuration, it is nearly impossible to generate good quality single block structured grids. Hence, flow simulation using a structured grid technology has to

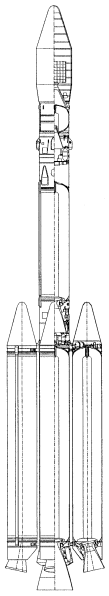

Fig. 1 Schematic representation of the complete VLS configuration.

resort to multiblock techniques. There is strong interest in the institutions here represented to develop the capability of numerically simulating flows over vehicles as complex as the VLS since this can reduce the need for wind tunnel tests, which typically have to be performed overseas in the Brazilian case. On the other hand, the interest for structured grids can be justified since most of the relevant physical problems that can arise in these vehicles are associated with turbulent flows and flow separation. For these cases, structured grids are usually more suitable and they produce better correlation with the experimental data.

The group has already developed a fair amount of experience in the simulation of axisymmetric flows relevant to the VLS operation and in the simulation of 3-D flows of isolated configurations[5]–[7]. However, this is the first attempt of calculating the flow over the complete vehicle. The decision was to use overset multiblock grids, *i.e.*, the *Chimera* approach[8]–[10]. The *Chimera* technique is a very useful tool in Computational Fluid Dynamics (CFD), since it offers more versatility for different types of problems with complex geometries. Hence, the objective of work here described is to extend the implementation, which was performed for the two-dimensional case by some of the present authors[11, 12], in order to develop the capability of simulating 3-D flows over the complete VLS configuration. The 3-D extension is validated considering a simpler problem, namely that of a cylinder inside a transonic convergent-divergent nozzle. Although this problem considers a 3-D formulation, its solution is actually 2-D for the case of an inviscid formulation. Hence, the calculations are compared to previous 2-D solutions for the problem, in the effort of validating the methodology implemented. The capability is, then, applied to flow simulations over the complete VLS vehicle. One should observe that the validation effort is an extremely important aspect of the present work, since there is no meaning in computing flows over such a realistic configuration without prior assessment of the correctness of the code at hand.

The flowfields of interest are assumed to be governed by the 3-D Euler equations. These equations are written in conservative form for general curvilinear coordinates and they are discretized in a structured, finite difference context. The spatial discretization scheme is based on central differences with the addition of scalar, non-isotropic artificial dissipation terms. This spatial discretization scheme is 2nd-order accurate in smooth regions of the flow. Time march uses an explicit, 5-stage, 2nd-order accurate Runge-Kutta time-stepping scheme. Convergence acceleration for steady state problems uses a variable time-stepping technique. One of the most important aspects in the implementation of a *Chimera* scheme concerns the interpolation of information across the various overlapping meshes. The interpolation process needs a previous analysis in order to define the neighboring points in the other meshes which will be used in this process, since it is necessary to identify all the boundary points in the overlapping region together with their neighboring points. Details of the particular interpolation scheme adopted in the present case are discussed in the paper. The forthcoming sections discuss the theoretical formulation together with the relevant aspects of the Chimera technique which are used in the present context. Validation results are presented for the simpler, convergent-divergent nozzle problem, and calculations for the complete VLS system are also presented and discussed.

2 Theoretical Formulation

2.1 Governing Equations

The flows of interest in the present work are simulated using the Euler equations in three dimensions. One can correctly state that actual flows over a configuration such as the VLS are necessary viscous and turbulent. However, in the interest of developing the capability of simulating such 3-D flows over complex, realistic configurations, there was a decision to limit the present investigation to inviscid flows. The 3-D Euler equations can be written in conservation-law

form for a curvilinear coordinate system as

$$\frac{\partial \overline{Q}}{\partial \tau}+\frac{\partial \overline{E}}{\partial \xi}+\frac{\partial \overline{F}}{\partial \eta}+\frac{\partial \overline{G}}{\partial \zeta}=0\,, \qquad (1)$$

where $\overline{Q}$ is the vector of conserved variables, defined as

$$\overline{Q}=J^{-1}\left[\rho,\rho u,\rho v,\rho w,e\right]^{T}\,. \qquad (2)$$

In these equations, ρ is the density, u, v and w are the Cartesian velocity components and e is the total energy per unit of volume. The $\overline{E}$, $\overline{F}$ and $\overline{G}$ are the inviscid flux vectors. For instance, $\overline{E}$ can be written as

$$\overline{E}=J^{-1}\left\{\begin{array}{c}\rho U\\ \rho uU+p\xi_x\\ \rho vU+p\xi_y\\ \rho wU+p\xi_z\\ (e+p)\,u-p\xi_t\end{array}\right\}\,, \qquad (3)$$

and similar expressions can be obtained[13] for $\overline{F}$ and $\overline{G}$. The expressions for the inviscid flux vectors in general curvilinear coordinates give rise to a new set of velocity components, the contravariant velocity components, which can be written as

$$\begin{aligned} U &= \xi_t+u\xi_x+v\xi_y+w\xi_z\,,\\ V &= \eta_t+u\eta_x+v\eta_y+w\eta_z\,,\\ W &= \zeta_t+u\zeta_x+v\zeta_y+w\zeta_z\,. \end{aligned} \qquad (4)$$

In the previous equations, J is the Jacobian of the transformation, which can be represented as

$$\begin{aligned} J &= \left(x_\xi y_\eta z_\zeta+x_\eta y_\zeta z_\xi+x_\zeta y_\xi z_\eta\right.\\ &- \left.x_\xi y_\zeta z_\eta-x_\eta y_\xi z_\zeta-x_\zeta y_\eta z_\xi\right)^{-1}\,. \end{aligned} \qquad (5)$$

Expressions for the various metric terms can be found in Ref. [13], among other references. The pressure can be obtained from the equation of state for a perfect gas as

$$p=(\gamma-1)\left[e-\frac{1}{2}\rho\left(u^2+v^2+w^2\right)\right]\,. \qquad (6)$$

A suitable nondimensionalization[14] of the governing equations has been assumed in order to write Eq. (1). In particular, the values of flow properties are made dimensionless with respect to freestream quantities, as described in Ref. [14].

2.2 Numerical Method

The governing equations were discretized in a finite difference context on structured hexahedral meshes which would conform to the bodies in the computational domain. Spatial derivatives are discretized using 3-point, central difference operators and, therefore, artificial dissipation terms must be added to the formulation in order to control nonlinear instabilities. The artificial dissipation terms used here are based on Turkel and Vatsa's scalar model[15]. This model is nonlinear and non-isotropic. The scaling of the artificial dissipation operator in each coordinate direction is weighted by the spectral radius of the corresponding flux Jacobian matrix, thus allowing for a better control of the explicitly added artificial dissipation terms. In the present implementation, the residue operator is defined as

$$\mathrm{RHS}^n=-\Delta t\left(\delta_\xi E^n+\delta_\eta F^n+\delta_\zeta G^n\right)\,, \qquad (7)$$

where E, F and G are numerical flux vectors. Here, the δ_ξ, δ_η and δ_ζ terms represent mid-point central difference operators in the ξ, η and ζ directions, respectively. The numerical flux vectors at the mesh mid-points are defined as

$$\begin{aligned} E_{i\pm1/2,j,k} &= \frac{1}{2}\left(\overline{E}_{i,j,k}+\overline{E}_{i\pm1,j,k}\right)\\ &- J^{-1}_{i\pm1/2,j,k}\,d_{i\pm1/2,j,k}\,,\\ F_{i,j\pm1/2,k} &= \frac{1}{2}\left(\overline{F}_{i,j,k}+\overline{F}_{i,j\pm1,k}\right)\\ &- J^{-1}_{i,j\pm1/2,k}\,d_{i,j\pm1/2,k}\,,\\ G_{i,j,k\pm1/2} &= \frac{1}{2}\left(\overline{G}_{i,j,k}+\overline{G}_{i,j,k\pm1}\right)\\ &- J^{-1}_{i,j,k\pm1/2}\,d_{i,j,k\pm1/2}\,. \end{aligned} \qquad (8)$$

The artificial dissipation operators, $d_{i\pm1/2,j,k}$, $d_{i,j\pm1/2,k}$ and $d_{i,j,k\pm1/2}$, are defined precisely as described in Ref. [15].

The time march is performed based on a 5-stage, 2nd-order accurate, hybrid Runge-Kutta

time-stepping scheme, where

$$\begin{aligned} \overline{Q}_i^{(0)} &= \overline{Q}_i^n \,, \\ \overline{Q}_i^{(\ell)} &= \overline{Q}_i^{(0)} - \alpha_\ell \mathrm{RHS}^{(\ell-1)} \,, \qquad \ell = 1, \ldots, 5 \,, \\ \overline{Q}_i^{n+1} &= \overline{Q}_i^{(5)} \,, \end{aligned} \tag{9}$$

and $\alpha_1 = \frac{1}{4}$, $\alpha_2 = \frac{1}{6}$, $\alpha_3 = \frac{3}{8}$, $\alpha_4 = \frac{1}{2}$ and $\alpha_5 = 1$. It should be emphasized that only the convective operator inside the RHS term indicated in Eq. (9) is actually evaluated at every time step. The artificial dissipation term is only evaluated in the first and second stages of the time-march procedure. It can be shown that this provides enough damping to maintain nonlinear stability[16] and, on the other hand, it yields a more efficient numerical scheme.

Since steady state solutions are the major interest of the present study, a variable time step convergence acceleration procedure has been implemented. In the present case, the time step is defined as

$$\Delta t_{i,j,k} = \frac{\mathrm{CFL}}{c_{i,j,k}} \,. \tag{10}$$

The characteristic velocity $c_{i,j,k}$ is defined as

$$\begin{aligned} c_{i,j,k} \;=\; \max \Big(& |U| + a\sqrt{\xi_x^2 + \xi_y^2 + \xi_z^2} \,, \\ & |V| + a\sqrt{\eta_x^2 + \eta_y^2 + \eta_z^2} \,, \\ & |W| + a\sqrt{\zeta_x^2 + \zeta_y^2 + \zeta_z^2} \Big)_{i,j,k} \,, \end{aligned} \tag{11}$$

where a is the speed of sound and U, V and W are the contravariant velocity components.

3 Details of the Chimera Implementation

The mesh point distribution over the physical domain in which the flow is to be computed is always a critical aspect for a successful calculation. Grid point distribution must be balanced enough to cover the entire flowfield, avoiding regions with excessive grid coarseness. On the other hand, points must be clustered in regions in which phenomena such as expansions and shock waves occur without exceeding the available computational resources. The computational

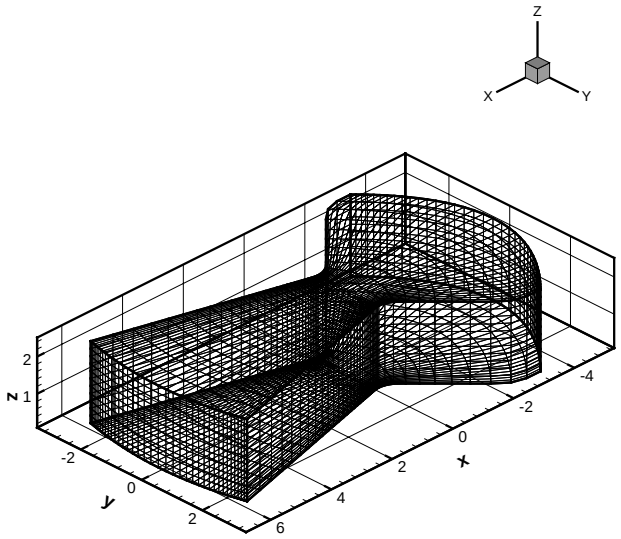

Fig. 2 Transonic convergent-divergent nozzle grid with $40 \times 37 \times 12$ points in the ξ, η and ζ directions, respectively.

meshes used in the present work were all generated by algebraic methods within each block. In particular, the multisurface algebraic grid generation technique described by Fletcher[17] has been implemented in a fairly general code for the rocket configurations. The code allows for grid clustering at various regions and for a fair amount of control in the grid point distribution along the normal direction. Both hyperbolic tangent and exponential grid stretching functions are used in order to obtain the desired grid clustering and coarsening over the body.

The convergent-divergent nozzle test case used two component meshes. The first mesh discretized the interior of the nozzle whereas the second one was the cylinder mesh. These individual grids are shown, respectively, in Figs. 2 and 3. For the complete VLS configuration, five component meshes were generated, one for each body which comprises the complete configuration. It should be emphasized that, although the present work is mainly concerned with Euler solutions, some of these meshes have a fair amount of grid stretching towards the wall. This is the result of an attempt to capture details of the shock reflection phenomena which are expected to occur in the cluster region of the VLS config-

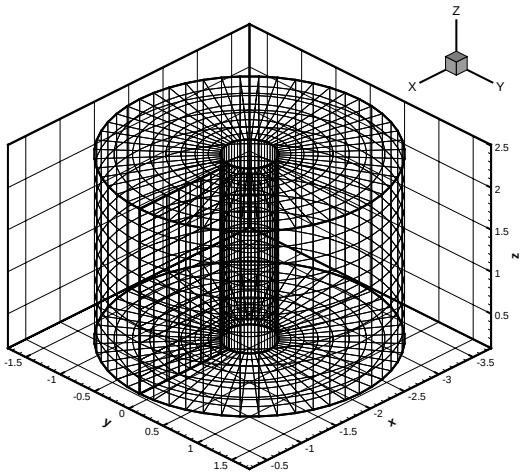

Fig. 3 Cylinder grid with $53 \times 9 \times 12$ points in the ξ, η and ζ directions, respectively.

uration. Another important aspect, still for the VLS case, is the need for a sufficiently large number of points between the lateral boosters and the central rocket body for an adequate behavior of the Chimera hole-cutting process. In this process, points of both meshes are eliminated from the set of active points in the domain either for being outside the flow region of interest or in order to avoid an excessively large region of overlap. This is performed with sufficient care in order to allow the formation of an interpolation area among the points of adjacent meshes. The existence of a larger number of points in those overlapping areas brings an improvement in the precision of the information exchange among the meshes at the expense of increasing the computational costs.

The present work uses trilinear interpolation in order to pass information at each mesh interior boundary point. It should be emphasized that there was no attempt to satisfy conservation in this interpolation process. Since shocks may be crossing the interface between grid blocks, it would be interesting to have the enforcement of some conservation statement at grid interfaces. However, this was not implemented in the present case due to the high computational costs associated with such an implementation, especially in the 3-D case, and because the present effort should be seen as an evolutionary step towards a more complete simulation capability. Furthermore, the use of a conservative interpolation process would certainly increase the code's memory requirements, which the authors would like to avoid at this time. A conservative method at the interfaces among Chimera meshes that satisfies the conservation laws was developed by Wang and Yang[18]. A detailed discussion of the approaches for handling these interior boundary conditions can be seen in Ref. [19].

The code which actually performs the hole-cutting process is a tool developed in-house by the group. The geometry of the computational domain is fairly simple in the convergent-divergent nozzle case. Therefore, the discussion that follows will try to concentrate on the VLS grid preparation. In the case of the VLS meshes, the code performs the logic elimination of the mesh points that are inside the other bodies and, therefore, out of the calculation domain. One of the meshes is treated as the primary mesh whereas the others are considered secondary meshes. In order to introduce the secondary meshes into the main mesh, a hole-cutting procedure is implemented. The size of the hole is determined by the size of the subdomain that must be fitted into the main mesh. Once the geometric parameters at a given interface are determined, and the neighborhood information is defined, one can concentrate in the particular application at hand. The solution process in the flow solver is essentially based on the following main steps:

1. Initial condition is imposed for all meshes;
2. The order of operation throughout the various meshes is defined;
3. The residue is calculated in the first mesh;
4. A new solution is calculated for the first mesh interior points;
5. Boundary conditions are updated for this first mesh;
6. The points along the hole boundary are updated in all meshes which have some overlapping with this first mesh;
7. The process is restarted from step (3) with the next mesh.

This process is repeated until all the meshes have reached the new solution level at time $(n+1)\Delta t$. Afterwards, convergence of the solution is verified. If the convergence criterion is not satisfied, the process is restarted from step (3).

4 Results and Discussion

4.1 Convergent-Divergent Nozzle Results

Two physical problems were studied in the present work. The first problem considers the flow in a transonic, convergent-divergent nozzle within which a circular cylinder is introduced. The calculations for this case were mostly intended to validate the simulation capability implemented. The cylinder was introduced in the convergent section of the nozzle for the present case, although previous 2-D flow calculations[12] have analyzed both the case in which the cylinder is in the convergent section and the case in which it is positioned in the divergent nozzle section. The computational domain is decomposed into two grid blocks for this case. The first block is the nozzle grid, indicated in Fig. 2, which is treated as the main grid for this case. The other block is formed by the cylinder grid, which is shown in Fig. 3. The nozzle grid has $40 \times 37 \times 12$ points in the longitudinal (ξ), contoured wall-normal (η) and depth (ζ) directions, respectively. The cylinder grid has $53 \times 9 \times 12$ points in the circumferential, wall-normal and depth directions, respectively. A view of a typical composite grid for this case can be seen in Fig. 4. All linear dimensions were normalized by the nozzle throat half height. The cylinder diameter was set to 0.3 length units, and the cylinder centerline was located along the nozzle longitudinal axis.

Several 3-D visualizations of inviscid flow solutions for this case, with the nozzle back pressure set low enough such that the flow is supersonic in the divergent section, were performed. As an example of the quality of the solutions obtained, Fig. 5 presents Mach number contours for this composite configuration. Other flow visualization plots for this test case are omitted for the sake of brevity. However, all scalar property

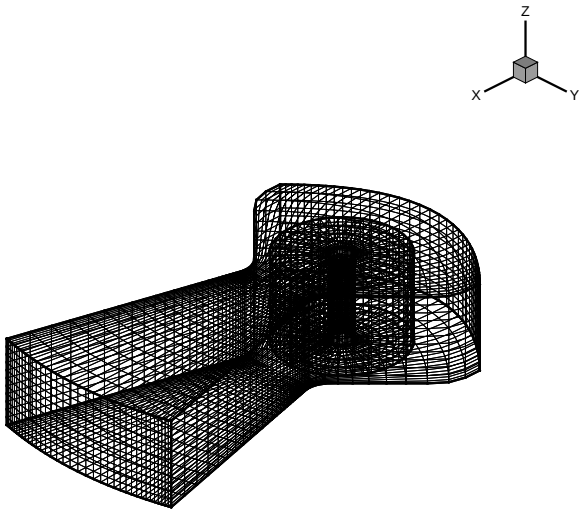

Fig. 4 Composite grid for cylinder inside the convergent section of a transonic convergent-divergent nozzle.

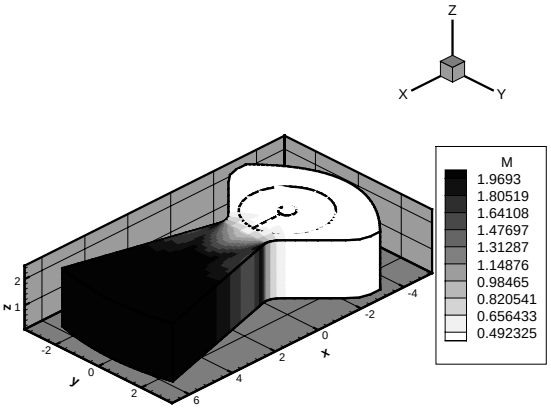

Fig. 5 Mach number contours for transonic convergent-divergent nozzle test case.

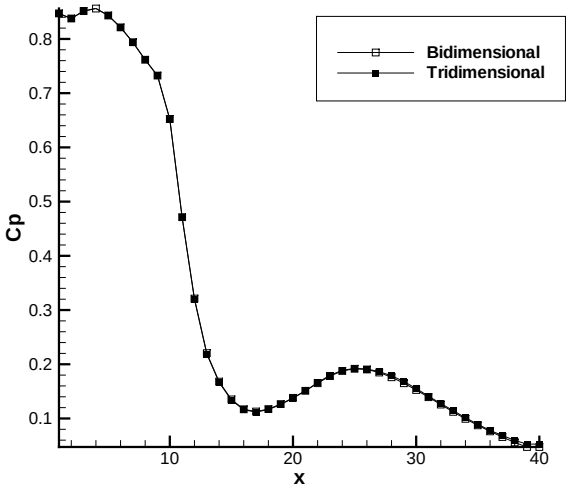

Fig. 6 Comparison of dimensionless wall pressure distributions for 2-D and 3-D calculations.

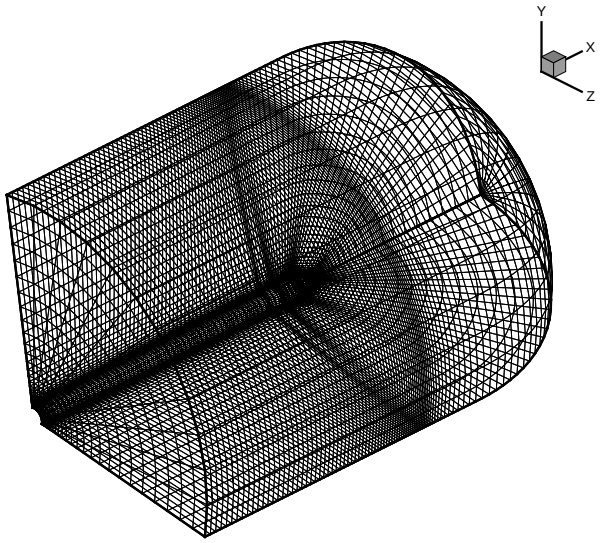

Fig. 7 Partial view of the central body mesh.

contour plots indicate good continuity of contour lines across the block interface. Similarly, velocity vector plots (not shown) also indicate good continuity of velocity vector orientations and magnitudes in the overlapping region. This is a very good indication of appropriate handling of the block interface communication as well as of the adequate implementation of the interpolation procedure. A comparison of the present 3-D results with those obtained for the 2-D case[12] indicate a perfect match. Clearly, one should observe that the present test case is actually a 2-D problem run with a 3-D grid, which essentially replicates the 2-D grid on 12 depth planes. Hence, its results should be identical to those of the 2-D problem described in Ref. [12]. Comparisons of flow properties along the nozzle contoured wall and centerline demonstrate this is indeed the case here. Hence, this validates the present 3-D implementation. As an indication of the type of agreement which is obtained between 2-D and 3-D results, Fig. 6 presents dimensionless pressure distributions along the contoured nozzle wall for both cases. As stated, it is clear that the results are a perfect match.

4.2 VLS Results

The other set of results here presented refers to simulations of the flow over the VLS vehicle during its first stage flight. The specific results included here consider only the case with freestream Mach number $M_\infty = 2$ and zero angle of attack, which is representative of the simulations performed so far for this configuration. Moreover, as the flight time in the lower atmosphere for these satellite launchers is very short and the vehicle is at supersonic speeds during most of this flight, it seems appropriate to select a supersonic flight condition for the present discussion. Furthermore, the purpose of the present paper lies mostly in the description of the capability implemented instead than a detailed account of the VLS aerodynamics.

The complete mesh system used in the present simulations was divided into 5 component meshes. One of these discretizes the computational domain around the central body using $120 \times 65 \times 33$ grid points in the longitudinal (ξ), wall-normal (η) and azimuthal (ζ) directions, respectively. The central body grid does not assume any symmetry in the vehicle and discretizes the complete central body. A partial view of this grid can be seen in Fig. 7. Four identical meshes are used for the boosters. Each of

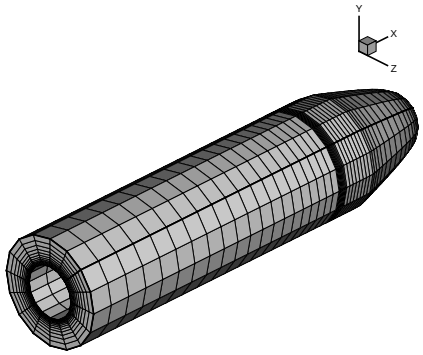

Fig. 8 Visualization of the complete grid for one booster.

them has $120 \times 36 \times 33$ grid points in the longitudinal, normal and circumferential directions, respectively. The grid for one booster can be seen in Fig. 8. Since only flow conditions at low incidence have been considered so far, one could use only half of this grid and impose symmetry conditions along the pitching plane for the present simulations. However, this has not been done here and the complete vehicle is represented. Moreover, as one can observe in Fig. 9, which represents one longitudinal plane of the complete grid which passes through the axes of the central body and two boosters, the afterbody portion of the vehicle has been simplified for the simulations here reported. One should compare the vehicle afterbody region as modeled in Figs. 7 and 9 with the schematic representation of the vehicle in Fig. 1. This simplification is performed because previous experience[3, 4] with afterbody flows has demonstrated the need for a viscous turbulent formulation for the adequate description of such flows. In the future, an accurate description of the afterbody will be included in the vehicle model, but this is beyond the scope of the present effort. Furthermore, the added complexity in the afterbody region would not contribute to the major interest of the present work.

Figure 10 presents a 3-D view of the VLS mesh, showing the body mesh for all 5 bodies and one longitudinal plane of the central body mesh together with the downstream plane for the same component grid. A detailed control of the grid point distribution for all meshes was exer-

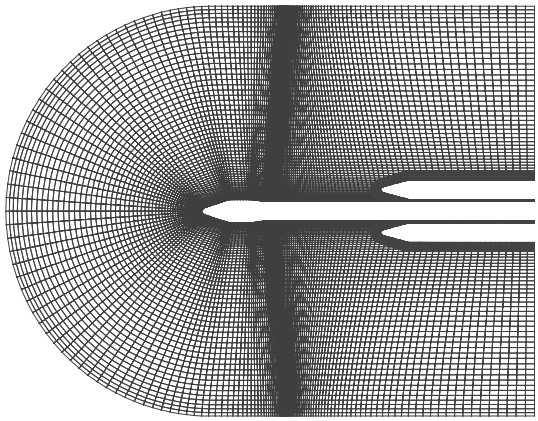

Fig. 9 Visualization of one longitudinal plane of the complete VLS configuration after the hole-cutting process. Particular plane selected includes two boosters.

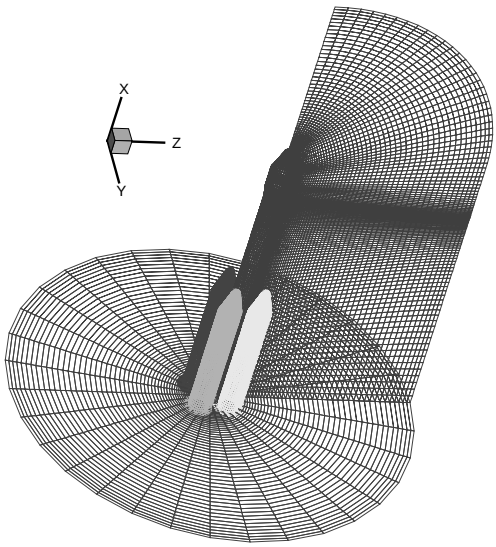

Fig. 10 Three-dimensional view of the complete VLS mesh.

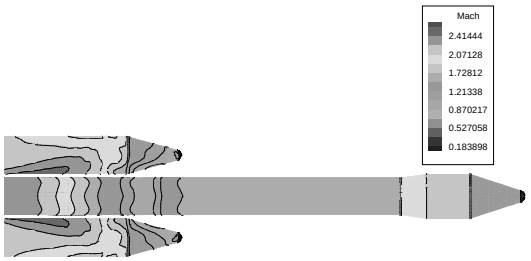

Fig. 11 Mach number contours on the central body and two opposing boosters for the VLS at $M_\infty = 2.0$ and zero angle of attack.

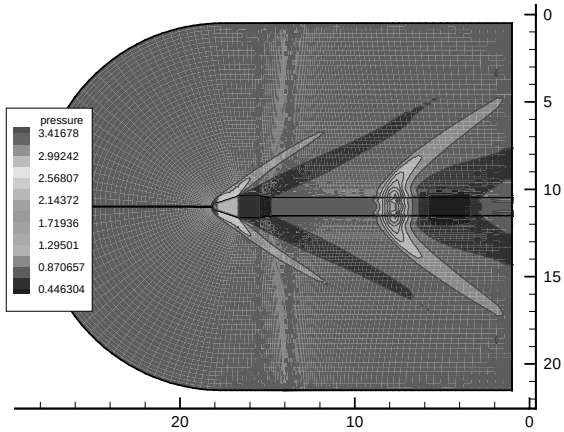

Fig. 12 Pressure contours for a longitudinal plane which does not include the boosters for $M_\infty = 2.0$, $\alpha = 0$ deg and azimuthal angle = 45 deg.

cised in order to guarantee a good concentration of points near the body solid walls. As previously discussed, although the present work is mainly concerned with Euler solutions, some of these meshes have a fair amount of grid stretching towards the wall. This is the result of an attempt to capture details of the shock reflection phenomena which are expected to occur in the cluster region. Another important factor is the concentration of points in the regions of grid overlap. It is important to guarantee a sufficiently large point concentration in these regions in order to try to minimize the errors from the interpolation process[19] among the various meshes. In particular, there was a definite attempt to guarantee a sufficiently large number of points between the lateral boosters and the central rocket body for an adequate behavior of the Chimera hole-cutting process.

Figure 11 exhibits Mach number contours along the surface of the central body and two of the boosters. One should observe that the booster that would be in front of the central body, considering a lateral view, has been removed in order to allow the visualization of the contours along the central core. The several regions affected by the detached shocks on the booster noses can be seen in Fig. 11. Moreover, one can also clearly see that the solution along the two boosters is symmetric, as one should expect for this zero angle of attack case.

The alternation of low and high speed regions indicated in Fig. 11 is associated to an alternation of high and low pressure regions, respectively, as indicated in Fig. 12. This figure shows pressure contours for a longitudinal plane along the vehicle which does not include any boosters. This longitudinal plane is formed by a cut in the complete mesh at an azimuthal position which is a symmetry plane between two boosters. The imprint on this plane of the previously described high and low pressure regions can also be clearly seen in Fig. 12. A similar visualization is indicated in Fig. 13, except that, in this case, a longitudinal plane which contains the central body and two boosters is selected. Both the solution in the field and the solution over the bodies is presented in the figure. The plots in both figures clearly indicate the bow shock wave ahead of the vehicle, the expansion which occurs at the forebody cone-cylinder intersection, the expansion region along the boattail, and the compression region ahead of the boosters. The complexity of the flow in the region of the boosters can also be appreciated in Fig. 13. It should be noted, however, that the grid resolution is not yet adequate to accurately capture the shock reflections between the central body and the boosters.

Figure 14 exhibits a comparison of the calculated pressure coefficient, Cp, distribution along the vehicle central body with the experimental data. In this case, a longitudinal plane which contains the central body and two booster axes is selected for the comparison. One can observe that the agreement in the forebody portion of the vehicle is very good. The agreement in the afterbody

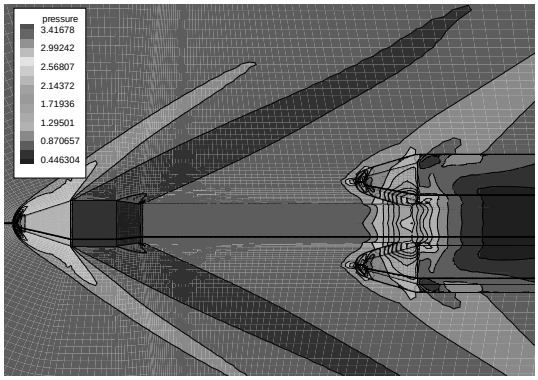

Fig. 13 Pressure contours for a longitudinal plane which passes through the axes of two boosters and central body ($M_\infty = 2.0$ and $\alpha = 0$ deg).

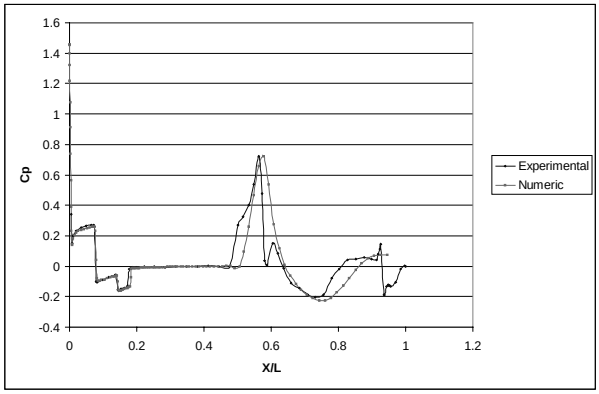

Fig. 14 Comparison of central body pressure coefficient distribution for a longitudinal plane in which there is a minimum distance between booster and central body ($M_\infty = 2.0$ and $\alpha = 0$ deg).

region, especially where there is a close proximity between central body and booster, is not as good. For instance, one can observe that the experimental data does indicate the reflection of the booster bow shock wave at x/L approximately equal to 0.6. Apparently, the grid resolution was not fine enough to capture this phenomenon in the numerical calculations. The striking difference in the results downstream of $x/L \cong 0.92$ is due to the fact that the central body nozzle was not modeled in the present calculations whereas it was present in the wind tunnel model. There is also a fair amount of difference in the Cp distributions in the $0.75 < x/L < 0.90$ range. It is believed that these differences are also due to the lack of resolution of the computational mesh in this region.

5 Concluding Remarks

The present paper is concerned with the development and validation of a 3-D flow simulation capability which would allow the calculation of flowfields over realistic launch vehicle configurations. The methodology is validated through the simulation of flows inside a 3-D convergent-divergent nozzle within which a cylinder has been inserted. Results for the nozzle flow have been presented and discussed for the case in which the cylinder is located in the convergent portion of the nozzle. A comparison of the present 3-D results for the nozzle has indicated very good agreement with previous 2-D calculations under the same conditions. The simulation capability is, then, applied to the study of flowfields over the VLS during its first-stage flight.

Test cases which consider supersonic flight for the VLS have been analyzed to date. The qualitative behavior of the numerical solution is very good for an Euler simulation. Agreement with experimental data is also very good in the forward portions of the vehicle, but the mesh clearly lacks refinement for a better resolution of the downstream portions of the flowfield. There was no apparent degradation of the quality of the flow solution due to the fact that there are shock

waves crossing the boundary between overset meshes. To the authors knowledge, this is the first time that such accurate and detailed simulations of the flow over the VLS are performed.

6 Acknowledgments

The present work was partially supported by Conselho Nacional de Desenvolvimento Científico e Tecnológico, CNPq, under the Integrated Project Research Grant No. 522413/96-0 and through graduate scholarships for the second and fourth authors. Additional support received from Fundação de Amparo à Pesquisa do Estado de São Paulo, FAPESP, in terms of a doctoral scholarship for the third author (Process No. 96/05003-0) is also gratefully acknowledged. The authors are also indebted to Núcleo de Atendimento em Computação de Alto Desempenho, NACAD-COPPE/UFRJ, which has provided the computational resources used for the present simulations.

References

[1] Azevedo, J.L.F., Menezes, J.C.L., and Fico, N.G.C.R., Jr. An assessment of boundary layer properties for transonic and supersonic flows over the VLS. AIAA Paper No. 95-1769-CP, 1995.

[2] Azevedo, J.L.F., Menezes, J.C.L., and Fico, N.G.C.R., Jr. Accurate turbulent calculations of transonic launch vehicle flows. AIAA Paper No. 96-2484-CP, June 1996.

[3] Azevedo, J.L.F., Strauss, D., and Ferrari, M.A.S. Viscous multiblock simulations of axisymmetric launch vehicle flows. AIAA Paper No. 97-2300-CP, June 1997.

[4] Strauss, D., and Azevedo, J.L.F. A numerical study of turbulent afterbody flows including a propulsive jet. AIAA Paper 99-3190, 1999.

[5] Azevedo, J.L.F., Zdravistch, F., and Silva, A.F.C. Implementation and validation of Euler solvers for launch vehicle flows. *Proceedings of the Fourth International Symposium on Computational Fluid Dynamics*, Vol. 1, Davis, CA, Sept. 1991, pp. 42-47.

[6] Azevedo, J.L.F., and Buonomo, C.A. Axisymmetric turbulent simulations of launch vehicle forebody flows. AIAA Paper No. 99-3528, 1999.

[7] Bigarelli, E.D.V., Mello, O.A.F., and Azevedo, J.L.F. Three dimensional flow simulations for typical launch vehicles at angle of attack. *Proceedings of the 15th Brazilian Congress of Mechanical Engineering*, Águas de Lindóia, SP, Brazil, Nov. 1999.

[8] Benek, J.A., Steger, J.L., and Dougherty, F.C. A flexible grid embedding technique with application to the Euler equations. AIAA Paper No. 83-1944-CP, 1983.

[9] Steger, J.L., Dougherty, F.C., and Benek, J.A. A Chimera grid scheme. *Advances in Grid Generation*, Vol. 5, ASME, New York, 1983.

[10] Benek, J.A., Buning, P.G., and Steger, J.L. A 3-D Chimera embedding technique. AIAA Paper No. 85-1523-CP, 1985.

[11] Yagua, L.C.Q., and Azevedo, J.L.F. Compressible flow simulation using overset multiblock grids. *Proceedings of the 4th Symposium on Overset Composite Grid & Solution Technology*, Vol. 1, Aberdeen, Maryland, Sept. 1998.

[12] Yagua, L.C.Q., Basso, E., and Azevedo, J.L.F. Overset mesh schemes for the two-dimensional compressible Euler equations. *Proceedings of the 7th Brazilian Congress of Engineering and Thermal Sciences*, Vol. 1, Rio de Janeiro, Brazil, Nov. 1998, pp. 1-6.

[13] Vieira, R., Azevedo, J.L.F., Fico, N.G.C.R., Jr., and Basso, E. Three dimensional flow simulation in the test section of a slotted transonic wind tunnel. *Proceedings of the 21st Congress of the International Council of the Aeronautical Sciences*, Melbourne, Australia, Sept. 1998.

[14] Pulliam, T.H., and Steger, J.L. Implicit finite-difference simulations of three-dimensional compressible flow. *AIAA Journal*, Vol. 18, No. 2, pp. 159-167, 1980.

[15] Turkel, E., and Vatsa, V.N. Effect of artificial viscosity on three-dimensional flow solutions. *AIAA Journal*, Vol. 32, No. 1, pp. 39-45, 1994.

[16] Jameson, A., Schmidt, W., and Turkel, E. Numerical solutions of the Euler equations by finite volume methods using Runge-Kutta time-stepping schemes. AIAA Paper No. 81-1259, June 1981.

[17] Fletcher, C.A.J. *Computational techniques for fluid dynamics*. 1st edition, Springer-Verlag, New York, 1988.

[18] Wang, Z.J., and Yang, H.Q. A unified conservative zonal interface treatment for arbitrarily patched and overlapped grids. AIAA Paper No. 94-0320, Jan. 1994.

[19] Wang, Z.J., Buning, P., and Benek, J. Critical evaluation of conservative and non-conservative interface treatment for Chimera grids. AIAA Paper No. 95-0077, Jan. 1995.